Identifying the Structure of Supported Metal Catalysts Using Vibrational Fingerprints from Ab Initio Nanoscale Models

*Agustin Salcedo[1], Deniz Zengel[2], Florian Maurer[2], Maria Casapu[2], Jan-Dierk Grunwaldt[2], Carine Michel[1], David Loffreda[*1]*

[1]ENS de Lyon, CNRS UMR 5182, Laboratoire de Chimie, 46 Allée d'Italie, 69364 Lyon, France

[2]Institute for Chemical Technology and Polymer Chemistry (ITCP), Karlsruhe Institute of Technology (KIT), Engesserstraße 20, 76131 Karlsruhe, Germany

Keywords

DRIFTS, DFT, Pd nanocatalysts, spectroscopy, ceria, carbon monoxide

Abstract

Identifying active sites of supported noble metal nanocatalysts remains challenging, since their size and shape undergo changes depending on the support, temperature, and gas mixture composition. Herein we simulate the anharmonic infrared spectrum of adsorbed CO using density functional theory (DFT) to gain insight into the nature of Pd nanoparticles (NPs) supported on ceria. We systematically determine how the simulated infrared spectra are affected by CO coverage, NP size (0.5–1.5 nm), NP morphology (octahedral, icosahedral), and metal-support contact angle, by exploring a diversity of realistic models inspired by *ab initio* molecular dynamics. The simulated spectra are then used as a spectroscopic fingerprint to characterize nanoparticles in a real catalyst, by comparison with *in situ* diffuse reflectance infrared Fourier transform spectroscopy (DRIFTS) experiments. Truncated octahedral NPs with an acute Pd-ceria angle reproduce most of the measurements. In particular, we isolate features characteristic of CO adsorbed at the metal-support interface appearing at low frequencies, both seen in simulation and experiment. This work illustrates the strong need for realistic models to provide a robust description of the active sites, especially at the interface of supported metal nanocatalysts, which can be highly dynamic and evolve considerably during reaction.

1. Introduction

The catalytic oxidation of methane plays a critical role in reducing the emissions of mobile and stationary sources, since the global warming potential of methane is more than 20 times higher than that of CO_2.[1,2] Among the various catalyst formulations tested so far, Pd-based nanocatalysts remain the most promising systems for methane removal. However, their activity below 400 °C is low, and their sensitivity toward water presence and sulfur poisoning is critical.[3–5] Insight into the catalyst structure, especially at the interface between metal and support, is required in order to improve their performance. In this sense, the contribution of Pd, PdO, or their mixture to the activity profile of Pd-based catalysts is still strongly debated.[6,7] Various Pd phases and nanoparticles can be created and stabilized by pre-treatment of the catalyst, tuning its performance. For instance, improved activity and stability were reported for pre-reduced ceria-supported catalysts[7–10] upon the formation of small Pd nanoparticles (NP).[11,12] The oxidation state, size, and shape of these noble metal nanoparticles can undergo changes depending on the support, temperature, and gas mixture composition.[6] Therefore, significant efforts must be conceded to elucidate the nanoscale nature of the relevant active phase of the catalyst.

Unraveling the structure of Pd nanoparticles remains challenging and requires a thorough characterization, for which complementary spectroscopy experiments and density functional theory (DFT) calculations constitute a powerful approach. Among possibilities, CO is a useful probe molecule for identifying the morphology of supported metallic nanocatalysts.[13,14] In this work, we perform DFT calculations to evaluate the scaled anharmonic stretching frequencies of CO molecules adsorbed on nanosized Pd/CeO_2 model systems and simulate their infrared spectra, to interpret those obtained by *in situ* diffuse reflectance infrared Fourier transform spectroscopy (DRIFTS). We develop this combined experimental and theoretical approach by using the

vibrational fingerprint of CO to identify the structure and coverage of supported palladium nanocatalysts. Typically, DFT studies reporting the stretching frequency of CO adsorbed on Pd restrict the analysis to simplified models such as extended Pd terraces[15] or Pd single atoms and very small clusters on oxide supports.[16–18] Recently, comprehensive first-principles computational studies of supported and unsupported Pd nanoparticles have been presented,[19–21] opening the door to calculations of the stretching frequency of CO adsorbed on such models. However, so far these works have restricted the scope to a single NP morphology and a single CO molecule, usually disregarding the impact of the support.[22–24] The variety of catalytic sites resulting from the morphology, structure, and size of the metallic nanoparticle and its interaction with an oxide support are usually neglected or only roughly approximated in the theoretical literature, but often invoked as critical by the experimental literature. Herein, Pd species generated in a reductively activated Pd/CeO_2 catalyst for methane oxidation are systematically addressed by examining CO adsorption on more realistic nanoscale theoretical models and comparing with experimentally obtained DRIFTS spectra.

2. Results and Discussion

The 2 wt.% Pd/CeO_2 catalyst used in this study contains metallic Pd nanoparticles with an average particle size of 1.7 nm (HAADF STEM/EDXS images in Figure 1a). These were obtained by an oxidative treatment at 800 °C in static air to completely redisperse Pd on the CeO_2 surface followed by a controlled pre-reductive treatment (see Experimental section). By this procedure, a relatively narrow particle size distribution was obtained, although very small particles in the sub-nanometer size range and larger up to 5 nm were observed as well. The resulting sample shows a

high methane oxidation activity at low temperatures, with already 50% CH_4 conversion at 291 °C in a gas mixture containing 3200 ppm CH_4, 10% O_2 in N_2 (Figure 1b).

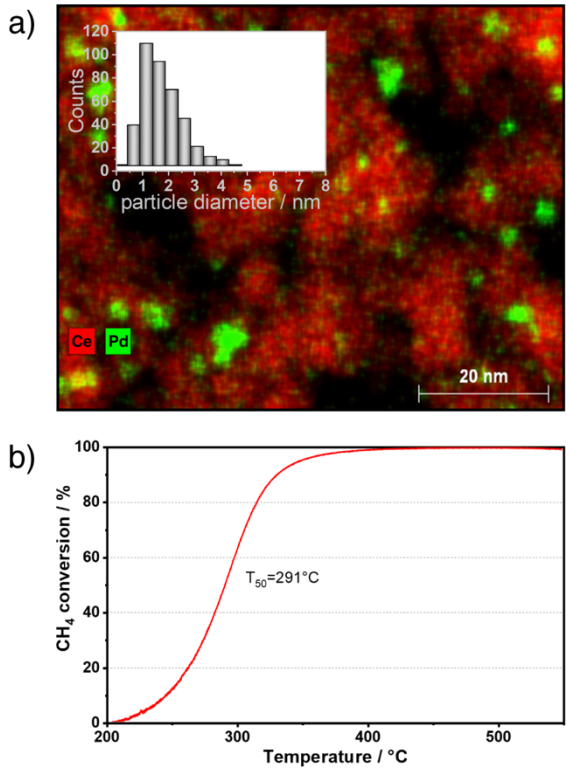

Figure 1. (a) HAADF-STEM/EDXS image and particle size distribution after reductive treatment. (b) CH_4 oxidation activity of 2 wt.% Pd/CeO_2 catalyst during light-off measurements (5 °C/min) in 1000 ppm CH_4, 8% O_2, and balance N_2.

CO was used as a probe molecule for DRIFTS investigations of the as-prepared catalyst (Figure 2a). The complementary calculated spectra were calculated for Pd_{147} model nanoparticles (~1.5 nm of diameter) covered with CO and supported on $CeO_2(111)$, the most stable low-index ceria termination[25]. The stoichiometric surface was considered, in line with the sample's exposure to air before characterization. Since the DRIFT spectrum was recorded at 30 °C, and linear CO is usually observed only at coverage close to saturation on extended Pd surfaces,[26–28] we set the CO

coverage to 0.75 monolayers (ML). A strongly irregular truncated octahedral (Pd_{147}sito) cluster was selected to model a wide variety of metallic coordination and CO adsorption sites (Figure 2b), since this nanocluster contains (100) and (111) facets of different sizes and shapes, namely hexagonal and pentagonal for (111) facets, and square and rectangular for (100) facets. Infrared (IR) spectra (Figure 2a) were simulated by calculating scaled anharmonic frequencies from harmonic vibrational analysis and evaluating the relative intensity of each normal mode as the square of the derivative of one component of the dipole moment of the catalyst model, which is perpendicular to the surface of the support (see Computational Details).

In the experimental spectrum, a distinct band separated by a valley is observed above 2000 cm^{-1} and deconvolved into two main peaks at 2081 and 2055 cm^{-1}. Below 2000 cm^{-1}, we observe a clear peak at 1972 cm^{-1}, followed by a broad band, which can be deconvolved into Gaussian curves at 1952, 1920, 1870 and 1810 cm^{-1}, and finally two distinct peaks at 1760 and 1695 cm^{-1}.

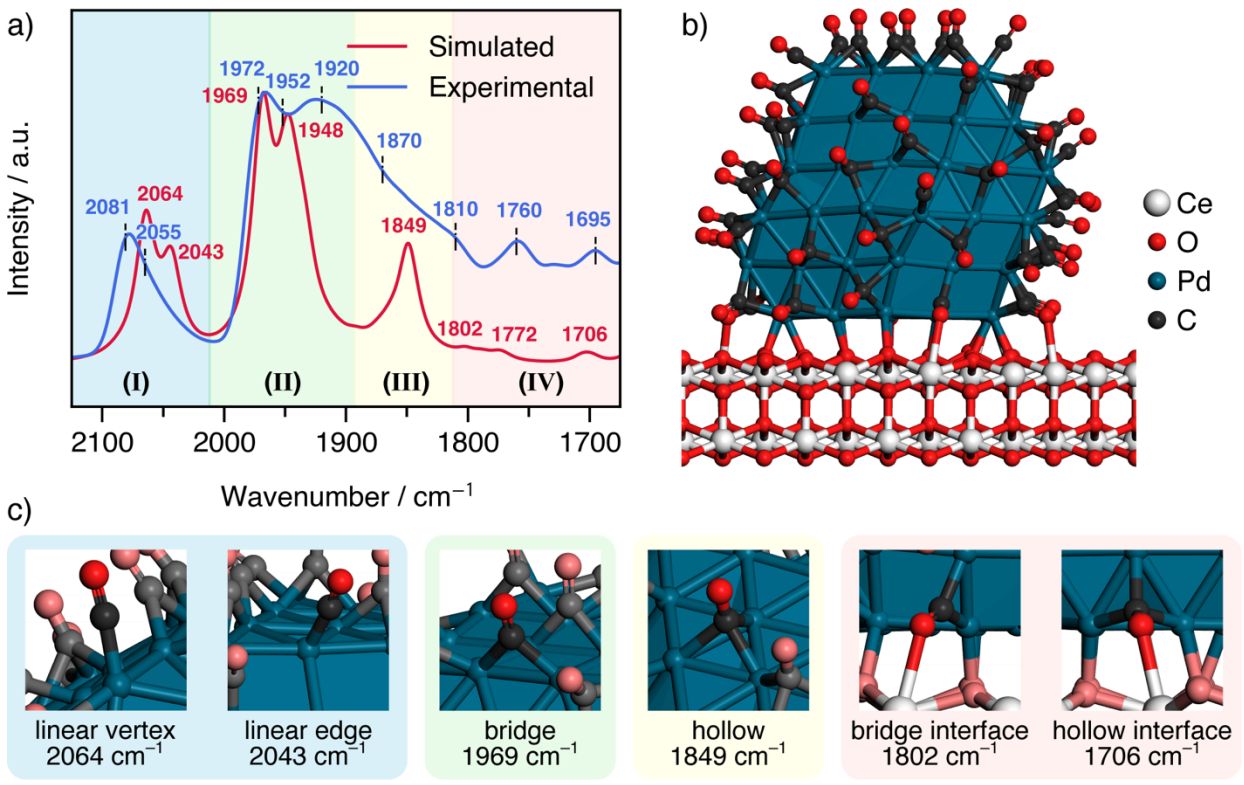

Figure 2. (a) DRIFT spectrum of the ceria-supported Pd catalyst after the reductive treatment, recorded in 1000 ppm CO at 303 K, together with the corresponding DFT-simulated IR spectrum, both normalized to unity at the maximum value. Frequencies obtained from deconvolution with Gaussian fits of the DRIFT spectrum are indicated. (b) DFT optimized structure of the catalyst model: Pd_{147}sito nanoparticle covered by 0.75 ML of CO and deposited on a pristine two trilayer CeO_2(111) slab. (c) Selected DFT-calculated scaled anharmonic frequencies and corresponding CO adsorption sites. Neighboring CO and surface oxygen are represented in lighter colors, to highlight the CO molecule on the indicated adsorption site.

By comparing with the DFT-simulated IR spectrum, we identify four main features labeled I–IV, as depicted in Figure 2a. The first feature (I) above 2000 cm^{-1} corresponds to linear CO, for which the simulated spectrum shows a peak at 2064 cm^{-1} associated with the vibration of CO on the

vertices of the NP, and one at 2043 cm^{-1} corresponding to linear CO on the edges of the NP (see Figure 2c for illustrations). These values are in good agreement with the experiments. Feature (II) corresponds to the peak at 1969 cm^{-1}, which matches the measured peak at 1972 cm^{-1} and is given by the symmetric vibration of multiple bridge-bound CO molecules on the truncated octahedral nanoparticle. The DFT calculation also gives other more anti-symmetric bridge modes, in which some CO molecules stretch in opposite phase. These are also IR-active in the specular mode and thus contribute to the spectrum (Table S1). Feature (III) corresponds to the experimental peak at 1870 cm^{-1} and can be interpreted by the calculated one at 1849 cm^{-1}, given by threefold hollow-bound CO molecules on (111) facets. Finally, feature (IV) given by the experimental peaks at 1810, 1760 and 1695 cm^{-1} can be assigned to CO molecules on bridge and hollow sites near the Pd-ceria interface, respectively, bound to Pd by the C atom and to Ce via the O atom. Such a bond to the ceria support weakens significantly the C–O bond, explaining the decrease (redshift) in the CO stretching frequencies. The DFT calculations for CO molecules at the Pd-ceria interface produce peaks for bridge CO in the range of 1772–1802 cm^{-1} and hollow CO at 1666–1706 cm^{-1} (Table S1), in good agreement with the experiments. Overall, the features observed in the experimental spectrum can be clearly identified in the DFT simulation, and the error with respect to the frequencies obtained by Gaussian deconvolution of the former is below 13 cm^{-1}. In addition, the presence of an oxygen vacancy at the vicinity of the ceria-supported Pd_{147}sito nanoparticle does not alter significantly the large majority of CO stretching frequencies (Table S10).

By considering a strongly irregular truncated octahedral Pd_{147}sito nanoparticle supported on CeO_2(111) at high CO coverage we obtain a good agreement with experiments, identifying the main vibrational bands in the DRIFT spectra. To evaluate the presence of competitive species and further assess the robustness of this model, we compare these vibrations with those calculated for

extended Pd surface slabs (representative of very large nanoparticles), and Pd single atoms, dimers, and trimers on CeO_2(111), which constitute the extreme models in terms of the number of Pd atoms. These comparisons highlight the importance of the holistic nanoscale approach that comprises the multiple states of a noble metal-based catalyst lifetime.

2.1. Extended flat surfaces and small clusters

Extended flat surface models cannot capture several features specific to nanoparticles such as the lower metallic coordination, the edges and kinks, the interaction with the support, and their finite nature. Furthermore, the dynamic coupling of stretching vibrations between neighbor CO molecules is maximized on flat terraces, thus shifting the vibrations towards higher frequencies. Therefore, although the (111) and (100) surface terminations are observed on nanoparticle facets, the extended terrace models are only representative of very large nanoparticles, where large flat facets dominate over edges and kinks. In line with this, we find that extended surface models do not reproduce the experimental IR spectrum of our Pd/CeO_2 catalyst containing mainly small nanoparticles. On the compact Pd(111) surface, CO adsorbs preferentially threefold on hollow fcc sites at low coverage, while at high coverage (0.75 ML), hollow CO is found to coexist with linear CO,[15] thus producing two peaks and coupled normal modes (Table S6). Bridge CO on the other hand is only found in a narrow window of coverages around 0.50 ML, and does not coexist with linear CO.[29] Furthermore, the calculated frequencies are too high in wavenumber compared to the experiments, with values of 2106 and 1897 cm^{-1} for linear and hollow CO, respectively (Table S6). This reflects that the interaction with the extended (111) surface does not destabilize the C–O bond sufficiently and the vibrational coupling between CO molecules is too strong, highlighting the need to consider a nanoparticle model. On the other hand, the Pd(100) surface is covered

exclusively with bridge CO even at a high coverage of 0.75 ML,[28,30] with a stretching frequency of 2028 cm^{-1}. In addition, none of these extended surfaces can explain the peaks at 1760 and 1695 cm^{-1}, which we have assigned to CO molecules adsorbed on Pd but concomitantly bound to the ceria support.

Regarding the presence of Pd single-atoms, previous works performing DFT calculations on Pd single-atoms adsorbed on CeO_2(111) reported frequencies of 2047, 2098 and 2137 cm^{-1} for Pd, PdO, and PdO_2, respectively.[16] Although at low Pd coverages we find similar frequencies, when the coverage is large enough the Pd single-atom model gives a frequency of 2078 cm^{-1} (Table S7). This indicates that a simple non-oxidized single-atom model is satisfactory to explain the peaks for linear CO observed in our experimental spectra, and therefore Pd single atoms could coexist with larger nanoparticles on the surface. Nevertheless, single-atom models are inadequate to explain the numerous bands below 2000 cm^{-1}, since they can only bind linear CO. We have considered dimer and trimer models as well, allowing bridge-bound CO, but we find that these do not properly reproduce the features observed in the experiment either (Table S7).

Having established the need to use a model consisting of a nanoparticle adsorbed on ceria to describe the Pd catalyst, we subsequently studied the effects of nanoparticle size and morphology, the contact angle at the metal-support interface, and the CO coverage on the simulated spectrum. Such exploration allows us to further determine the relevance of our interpretation and the robustness of our theoretical analysis.

2.2. Effect of size and morphology

We considered the effect of size by comparing with a Pd_{13} cluster of about 0.8 nm, representing the sub-nanometer clusters observed by microscopy. Due to the large fluxionality at this size, the

structure of the cluster was optimized via canonical sampling through velocity rescaling, from three different seeds. Details can be found in the Supporting Information. The resulting structure (Figure 3a) is a bilayer cluster (9+4) covered mostly with hollow CO, but with some linear and bridge CO as well. Linear CO appears in the computed spectrum at 2043 cm^{-1}, similar to single atoms and Pd_{147}sito. However, bridge and hollow CO appear at 1900 and 1868 cm^{-1} respectively (Figure 3b), where no feature was observed for the Pd_{147}sito nanoparticle. Therefore, these results complement the ones for Pd_{147}sito, and help explain the broad band that spans over the whole frequency range, observed by DRIFTS. Overall, the statistical contribution of NPs of various sizes and different co-adsorption configurations might explain the continuous nature of the band recorded in the experiment.

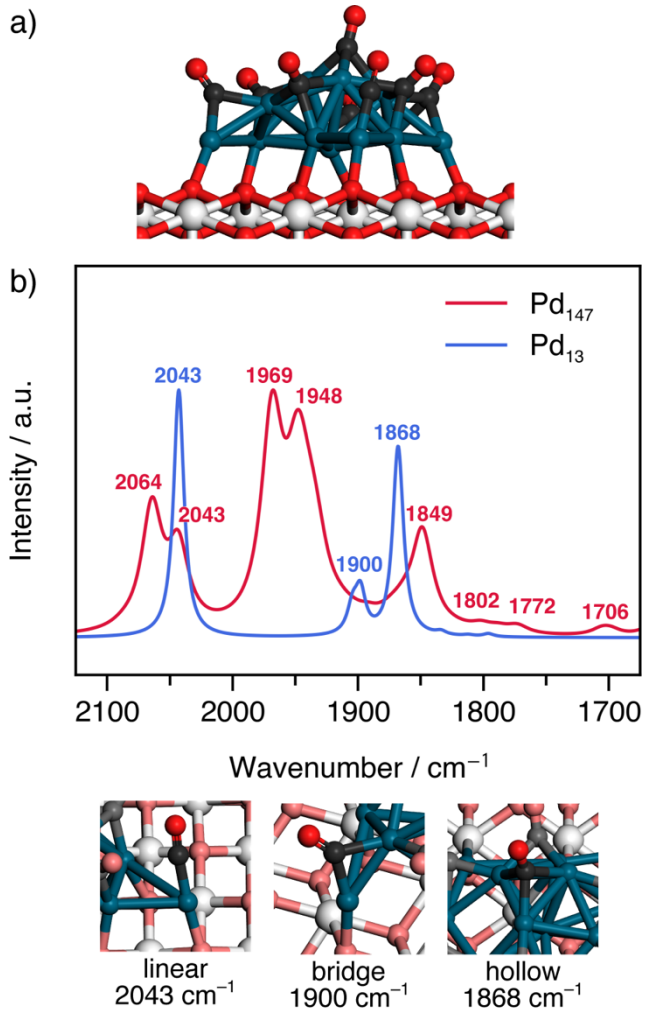

Figure 3. Size effect. (a) DFT optimized structure of Pd_{13} on pristine $CeO_2(111)$ covered with CO. (b) DFT-simulated IR spectra for strongly irregular truncated octahedral Pd_{147}sito and Pd_{13} nanoparticles covered with CO and supported on pristine $CeO_2(111)$, both normalized to unity at the maximum value. Selected DFT-calculated frequencies and corresponding CO adsorption sites are shown below. Neighboring CO and surface oxygen are represented in lighter colors, to highlight the CO molecule on the indicated adsorption site.

Regarding the nanoparticle morphology, the previously discussed truncated octahedron (Pd_{147}sito), which provides a good agreement with experiments, presents (100)-type facets and

(100)–(111) edges that favor bridge-bound CO, resulting in the peak appearing at 1969 cm^{-1}. But it also offers large (111) facets, which are dominated by hollow CO, and therefore are at the origin of peaks in the range of 1800–1900 cm^{-1} (Figure 2a). To consider the effect of the morphology change we compared the spectrum with that of a competitive structural isomer, namely a Pd_{147} icosahedron (Pd_{147}ico). Our DFT calculations indicate that the icosahedron is less stable in vacuum than the truncated octahedron, but only by 27 $kJ.mol^{-1}$. Hence, they could coexist depending on the temperature and coverage. However, the icosahedron structure is exclusively composed of (111) facets, which favor hollow CO, even for CO molecules close to the edges of the nanoparticle, where hollow hcp sites are preferred over bridge sites (Table S8). Therefore, the icosahedral structure cannot explain the peak at 1972 cm^{-1} associated with bridge CO, as shown in Figure 4.

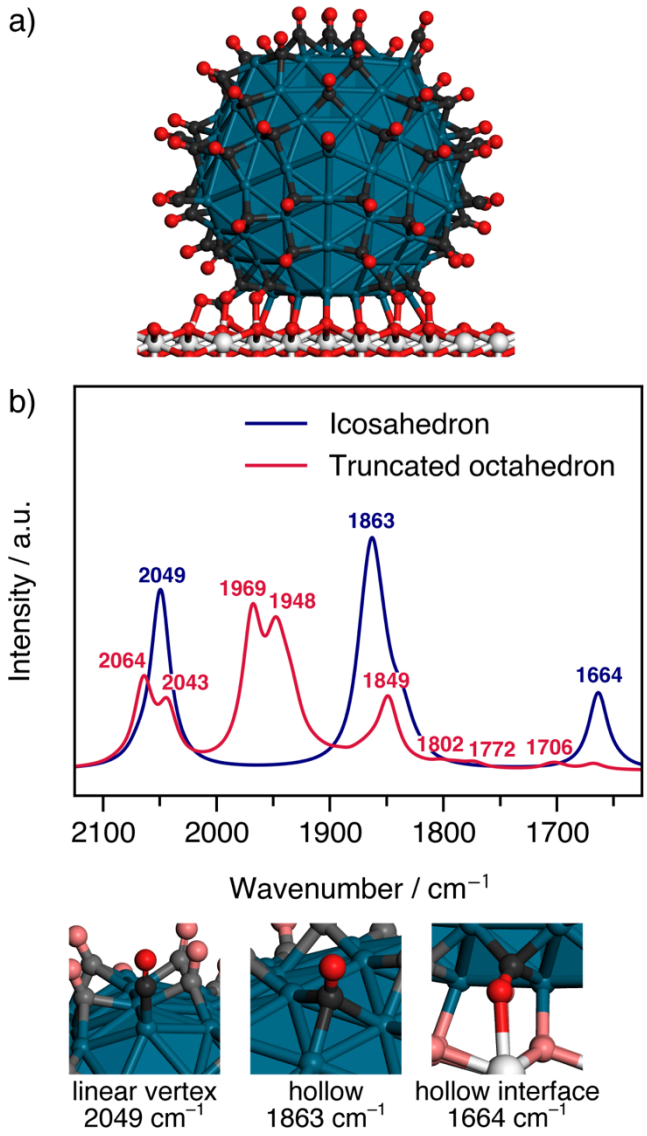

Figure 4. Morphological effect. (a) DFT optimized structure of Pd_{147}ico on pristine CeO_2(111) covered with 0.75 ML of CO. (b) DFT-simulated IR spectra for strongly irregular truncated octahedral Pd_{147}sito and icosahedral Pd_{147}ico nanoparticles covered with 0.75 ML of CO and supported on pristine CeO_2(111). Selected DFT-calculated frequencies and corresponding CO adsorption sites are shown below. Neighboring CO and surface oxygen are represented in lighter colors, to highlight the CO molecule on the indicated adsorption site.

The DFT simulation predicts three main distinguishable peaks. The first one corresponds to linear CO at vertices (linear CO at edges was not considered in this model), with an intense mode at 2049 cm^{-1}, and lower intensity contributions at 2053 and 2069 cm^{-1} (Figure 4, Table S3). The second peak is a convolution of hollow modes, in the range 1838–1871 cm^{-1}. Finally, hollow CO bound to ceria at the Pd-ceria interface appears at ~1664 cm^{-1}, a range masked by carbonates in the experimental spectrum. Overall, the presence of icosahedral NP cannot be discarded since it gives frequencies consistent with the experiment, but their concentration should be negligible compared to that of truncated octahedral NPs, since the most intense peak ascribed to bridge CO is absent for the icosahedral morphology.

2.3. Effect of the metal-support interface

To evaluate the effect of the contact angle we generated a "hemispherical" $Pd_{79}/CeO_2(111)$ model, consisting of half of the truncated octahedral Pd_{147}sito nanoparticle covered with 0.75 ML of CO, deposited on the $CeO_2(111)$ surface (Figure 5a, right). The NP is cut at the widest part so that its diameter remains the same, matching the experimental value. This adsorbed truncated cluster is only 11 kJ per mole of Pd higher in formation energy than the supported spherical nanoparticle. We observe that the spectrum for the hemispherical NP compares well with the one for spherical nanoparticle for the most part, except for the low-frequency peaks below 1810 cm^{-1} previously assigned to CO at the Pd-ceria interface, which are not reproduced by the hemispherical model (Figure 5b). This can be understood by looking at the orientation of the CO molecules at the interface. In the hemispherical NP the obtuse contact angle (~110–130°) is such that CO molecules on hollow sites at the interface point away from the support, and therefore cannot form the bond with ceria that would lower the stretching frequency (the OCO–Ce distances are greater

than 3 Å). To form a bond with Ce cations, CO molecules must bind twofold on the edge of the hemispherical NP and adopt an orientation parallel to the surface, but this results in non-IR active stretching modes. On the other hand, the acute angle between the spherical nanoparticle and ceria (~60–70°) allows the formation of IR active CO species bound to both Pd and ceria (i.e. vibrating with a component perpendicular to the surface). Such CO species show CO–Ce distances shorter than 2.85 Å (Figure 5c), and intramolecular C–O bond lengths increased by about 0.02 Å with respect to CO molecules bound only to Pd. This suggests that an acute contact angle allows the IR-active low-frequency vibrations corresponding to CO molecules interacting with the support.

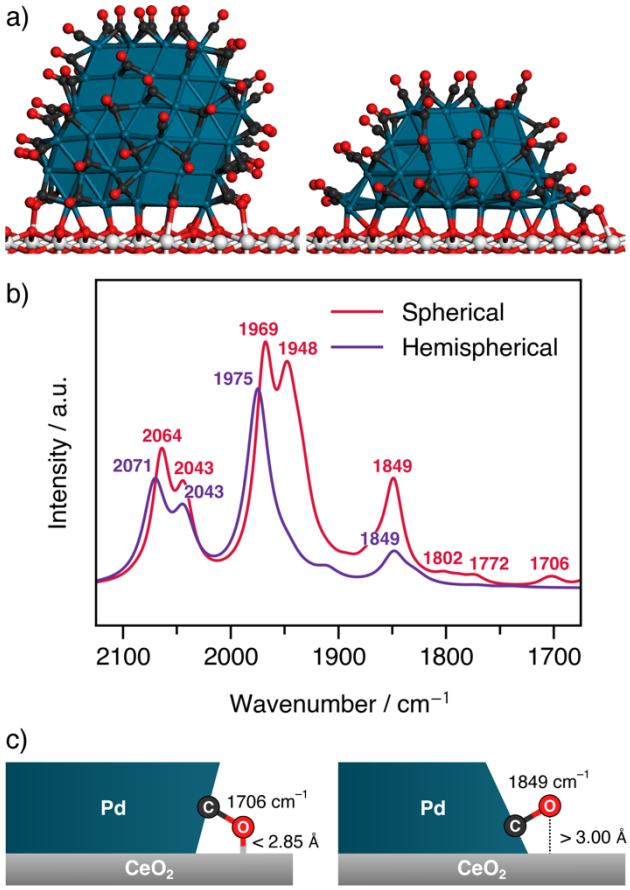

Figure 5. Contact angle effect. (a) Optimized structures of Pd_{147}sito (left) and truncated sito Pd_{79} (right) nanoparticles covered with 0.75 ML of CO adsorbed on pristine CeO_2(111), constituting

spherical and hemispherical models, respectively. (b) DFT-simulated IR spectra for both systems. (c) Scheme illustrating the difference in the adsorption of CO on hollow sites at the Pd-ceria interface between spherical and hemispherical models.

2.4. Effect of the CO coverage

Finally, we considered the effect of CO coverage by calculating the simulated IR spectrum for the truncated octahedral nanoparticle at 0.25 ML (Figure 6a). At this low coverage no linear CO should be present, since single Pd atoms are not the most favorable adsorption sites for isolated CO (Table S8), in line with experiments and calculations for CO adsorption on Pd thin films.[28–32]

We generated this model by adsorbing CO exclusively on the most favorable sites, namely bridge sites at edges. Therefore, the spectrum shows no peak corresponding to linear and hollow CO, and the main peak representative of bridge CO is shifted down by 67 cm^{-1}, reducing significantly the agreement with the experiments (Figure 6b). The frequencies calculated in the range 1758–1795 cm^{-1} are assigned to bridge-bonded CO at the Pd-ceria interface. Another range of computed frequencies at 1636–1668 cm^{-1} is also observed and corresponds to CO molecules at the interface that have moved from initial bridge sites to hollow sites. This comparison highlights the importance of considering a strong vibrational coupling between various CO adsorbates at a sufficiently high coverage to spread the CO stretching vibrational region into several IR active bands.

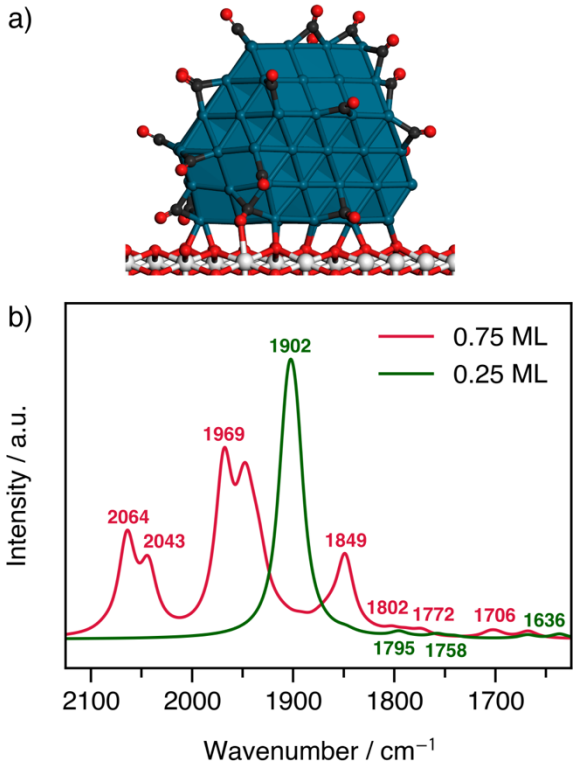

Figure 6. Adsorbate coverage effect. (a) Structure of truncated octahedral Pd_{147}sito covered with 0.25 ML of CO adsorbed on CeO_2(111). (b) DFT-simulated IR spectra, compared to the one obtained for the same NP with a CO coverage of 0.75 ML.

3. Conclusions

Overall, we have used the vibrational fingerprints of CO molecules obtained from DFT-simulated infrared spectra to identify the nature of the adsorption sites and the structure of a Pd/CeO_2 catalyst for methane oxidation comprised mainly of small noble metal nanoparticles. We demonstrate the need to consider nanoscale models of supported palladium to correctly reproduce the experimental CO adsorption DRIFT spectra, as opposed to usual models such as extended Pd surfaces or very small (1–3 atom) clusters adsorbed on ceria. We also show the impact of coverage

effects in the calculated frequencies, highlighting the importance of considering various coverages when comparing with experiments.

Furthermore, by comparing different morphologies, we observe that the Pd nanoparticles of ~1.5 nm of diameter formed in the catalyst most probably expose both (111)- and (100)-type facets, since the presence of the latter explains the intense peak at 1972 cm^{-1} associated to bridge CO. Sub-nanometer particles are also likely to contribute to the observed spectrum. Moreover, we find indications that an acute contact angle, usually associated with relatively weak metal-support interactions, provides relevant adsorption sites to explain the low-frequency vibrations under 1800 cm^{-1}. The high CH_4 oxidation activity at low temperatures seems to be promoted by the presence of such faceted Pd nanoparticles. The formation of reactive PdO_x is expected during exposure of such particles to reaction mixture,[7] but as shown in this study, the noble metal-CeO_2 interface sites could also be involved in the mechanism. Overall, this combined experimental and theoretical spectroscopic study opens promising perspectives for improving our ability to characterize the interfacial active sites of supported metallic nanocatalysts under relevant reaction conditions by using a probe molecule such as CO.

4. Methods

4.1. Experimental

Catalyst preparation: the 2 wt.% Pd/CeO_2 catalyst was prepared by incipient wetness impregnation of commercial CeO_2 (Solvay) with an aqueous solution of tetraamine palladium(II) nitrate (5 wt.% Pd, 99.9% purity, abcr), followed by drying and calcination for 10 h in static air at 800 °C. This treatment resulted in the formation of highly dispersed noble metal species.[33] To

obtain Pd nanoparticles the resulting sample was reduced in 5% H_2/N_2 at 500 °C for 1 h and afterwards cooled in an inert atmosphere. The as prepared catalyst was exposed to the ambient atmosphere before further characterization.

Catalyst characterization: N_2-physisorption measurements were conducted using a BELSORP Mini II analyzer (MicrotracBEL) and indicate a BET surface area (Brunauer-Emmett-Teller method) of 122 m^2/g. The particle size distribution of the noble metal particles was evaluated with the software package Fiji by analysis of >300 noble metal particles from scanning transmission electron microscopy (STEM) images with EDXS-mapping. The electron microscopy data were obtained on a FEI OSIRIS microscope (200 kV electron energy) at the Laboratory for Electron Microscopy (KIT) in the high-angle annular dark field scanning (HAADF) mode.

Catalytic tests: CH_4 oxidation measurements were conducted on an in-house built catalyst test bench at the Exhaust Center Karlsruhe (KIT). A quartz plug-flow reactor was loaded with sieved fractions of 300 mg of catalyst powder diluted with 700 mg of quartz sand (both 125–250 μm). Mass flow controllers (Bronkhorst) were used to dose a gas mixture containing 3200 ppm CH_4, 10% O_2 in N_2 with 1 L/min flow. Reaction gases were analyzed by an online Fourier-transform infrared spectrometer (FTIR, Multigas MG2030, MKS) during heating up the catalyst bed with 5 K/min between 200–550 °C.

Diffuse reflectance infrared Fourier transform spectroscopy (DRIFTS) data were recorded on a Bruker VERTEX 70 spectrometer equipped with an *in situ* cell (Harrick). The sample powder was used in a sieve fraction 125–250 μm and pre-treated in an inert atmosphere (Ar) by heating to 250 °C. CO adsorption was investigated upon dosing 200 ml/min of 1000 ppm CO/Ar at 30 °C over the sample. The CO concentration was chosen to limit the noble metal restructuring.[34] The gas

composition at the exit of the cell was continuously analyzed with a mass spectrometer (Pfeiffer Vacuum).

4.2. Computational Details

Density functional theory (DFT) calculations were performed using the VASP code.[35,36] The exchange-correlation energy was calculated within the generalized gradient approximation (GGA), with the Perdew–Burke–Ernzerhof (PBE) exchange-correlation functional.[37] Long-range dispersion corrections were implemented using the DFT-D3(BJ) functional.[38,39] The valence electrons were treated on a plane-wave basis with an energy cutoff of 400 eV, whereas the core electrons were represented with the projector-augmented wave (PAW) method.[40,41] Total energies were calculated with a numeric precision of 10^{-6} eV. The DFT+U approach was implemented within Dudarev's scheme,[42] to consider strong electronic correlation effects due to charge localization and compensate for the self-interaction error,[25,43–46] with U_{eff} set to 4.5 eV.[47,48] The forces were converged to ±0.02 eV/Å. The Brillouin zone was sampled at the gamma point only.

The $CeO_2(111)$ surface was modeled using a (6×6) supercell, generated from a ceria bulk with the equilibrium lattice parameter of a_0 = 5.455 Å, and consisting of 6 atomic layers (two O–Ce–O trilayers, TL) separated by a 23 Å thick vacuum-layer. The atoms in the bottom TL were kept frozen in their bulk positions, while those belonging to the uppermost TL were relaxed. At this size, the distance parallel to the surface between the geometric center of a Pd nanoparticle and that of its first periodic replica is about 50% larger than the nanoparticle diameter, preventing their interaction. Smaller supercells of (2×2) and (3×3) were used for $Pd_{1–3}$ clusters, and (4×4) for Pd_{13} clusters.

The low CO coverage model was generated by placing CO on the most favorable adsorption site. High coverage models were designed by starting from 1 ML and removing a fraction of the CO molecules. Several randomly generated configurations were obtained this way, and the one with lowest energy was further improved by *ab initio* molecular dynamics using canonical sampling through a velocity rescaling thermostat at 1000 K.[49] These calculations were run with the CP2K code to speed up the screening, with a Double-ζ Gaussian basis set and an auxiliary plane wave basis (GPW approach).[50,51] Low energy structures were quenched to 0 K by using VASP and compared with the randomly generated initial structure. All the degrees of freedom of supported and CO-covered Pd nanoparticles have been systematically relaxed.

Harmonic vibrational frequencies and normal modes were obtained by diagonalization of the Hessian matrix, with force constants obtained from finite differences with atomic displacements of 0.02 Å in the positions of the CO molecules. Anharmonic corrections were introduced by fitting the potential energy around the equilibrium state in the space of the normal coordinates with a third-order development of the Morse potential. In addition, all frequencies have been scaled by a factor of 1.0224, chosen so that the calculated stretching frequency of gas-phase CO matches perfectly the experimental value (2143 cm^{-1}).

The infrared intensities I^k for each normal mode Q_k are proportional to the square of the derivate of the component of the dynamic dipole moment perpendicular to the surface (μ_Z), following the selection rules of DRIFTS. To obtain this value, the derivatives of μ_Z in the 3*N* Cartesian coordinates r_i are evaluated by finite differences and then multiplied by the components of the mass-weighted coordinate matrix of the vibrational modes $P_{ki}/(m_i)^{1/2}$.

$$I^k \propto \left(\frac{\mathrm{d}\mu_Z}{\mathrm{d}Q_k}\right)^2 = \left(\sum_i^{3N} \frac{P_{ki}}{\sqrt{m_i}} \frac{\partial \mu_Z}{\partial r_i}\right)^2$$

The simulated spectra were plotted by convolving the DFT-calculated intensities with Lorentzian functions (full width at half maximum = 20 cm^{-1}).

Supporting Information

Generation of Pd_{13} clusters supported on $CeO_2(111)$ (structures in vacuum presented in Figure S1, *ab initio* molecular dynamics simulations, trajectories and 0 K quenched final structures, exposed in Figure S2). Complete list of vibrational frequencies of CO for all the systems studied (Tables S1–S7). Adsorption energy of isolated CO molecules on selected sites (Table S8). Adsorption energy of Pd nanoparticles on $CeO_2(111)$ (Table S9). Comparative analysis of harmonic CO stretching frequencies for CO-covered Pd_{147}sito nanoparticle supported on stoichiometric and reduced ceria (single oxygen vacancy at the vicinity of the cluster) (Table S10).

Acknowledgments

The authors acknowledge financial support from Agence National de la Recherche (ANR-19-CE05-0038, PRCI DYCAT project) and the Deutsche Forschungsgemeinschaft (DFG, German Research Foundation; 431423888 DYCAT project). The authors thank PSMN (Data Center) in Lyon for CPU time and assistance, GENCI resources and the CPER/SYSPROD 2015–2022 project (N°2019-AURA-P5B) for financial support. Furthermore, we thank H. Störmer (LEM, KIT) for TEM measurements and the Deutsche Forschungsgemeinschaft for supplementary funding of this project (DFG, German Research Foundation) – SFB 1441 – Project-ID 426888090.

References

[1] B. Wang, S. Albarracín-Suazo, Y. Pagán-Torres, E. Nikolla, *Catal Today* **2017**, *285*, 147.

[2] M. Monai, T. Montini, R. J. Gorte, P. Fornasiero, *Eur J Inorg Chem* **2018**, *2018*, 2884.

[3] A. Gremminger, P. Lott, M. Merts, M. Casapu, J.-D. Grunwaldt, O. Deutschmann, *Appl Catal B* **2017**, *218*, 833.

[4] A. T. Gremminger, H. W. Pereira de Carvalho, R. Popescu, J.-D. Grunwaldt, O. Deutschmann, *Catal Today* **2015**, *258*, 470.

[5] J. Chen, H. Arandiyan, X. Gao, J. Li, *Catalysis Surveys from Asia* **2015**, *19*, 140.

[6] D. Ciuparu, M. R. Lyubovsky, E. Altman, L. D. Pfefferle, A. Datye, *Catalysis Reviews* **2002**, *44*, 593.

[7] P. Lott, P. Dolcet, M. Casapu, J.-D. Grunwaldt, O. Deutschmann, *Ind Eng Chem Res* **2019**, *58*, 12561.

[8] R. Burch, F. J. Urbano, *Appl Catal A Gen* **1995**, *124*, 121.

[9] C. A. Müller, M. Maciejewski, R. A. Koeppel, A. Baiker, *Catal Today* **1999**, *47*, 245.

[10] H. Xiong, M. H. Wiebenga, C. Carrillo, J. R. Gaudet, H. N. Pham, D. Kunwar, S. H. Oh, G. Qi, C. H. Kim, A. K. Datye, *Appl Catal B* **2018**, *236*, 436.

[11] S. Colussi, A. Gayen, M. Farnesi Camellone, M. Boaro, J. Llorca, S. Fabris, A. Trovarelli, *Angewandte Chemie International Edition* **2009**, *48*, 8481.

[12] M. Cargnello, J. J. D. Jaén, J. C. H. Garrido, K. Bakhmutsky, T. Montini, J. J. C. Gámez, R. J. Gorte, P. Fornasiero, *Science (1979)* **2012**, *337*, 713.

[13] G. M. Lari, E. Nowicka, D. J. Morgan, S. A. Kondrat, G. J. Hutchings, *Physical Chemistry Chemical Physics* **2015**, *17*, 23236.

[14] A. Tereshchenko, A. Guda, V. Polyakov, Y. Rusalev, V. Butova, A. Soldatov, *Analyst* **2020**, *145*, 7534.

[15] D. Loffreda, D. Simon, P. Sautet, *Surf Sci* **1999**, *425*, 68.

[16] G. Spezzati, Y. Su, J. P. Hofmann, A. D. Benavidez, A. T. DeLaRiva, J. McCabe, A. K. Datye, E. J. M. Hensen, *ACS Catal* **2017**, *7*, 6887.

[17] V. Muravev, G. Spezzati, Y.-Q. Su, A. Parastaev, F.-K. Chiang, A. Longo, C. Escudero, N. Kosinov, E. J. M. Hensen, *Nat Catal* **2021**, *4*, 469.

[18] V. Muravev, J. F. M. Simons, A. Parastaev, M. A. Verheijen, J. J. C. Struijs, N. Kosinov, E. J. M. Hensen, *Angewandte Chemie International Edition* **2022**, *61*, DOI 10.1002/anie.202200434.

[19] L. Vega, F. Viñes, K. M. Neyman, *Nanomaterials* **2021**, *12*, 17.

[20] S. M. Kozlov, H. A. Aleksandrov, J. Goniakowski, K. M. Neyman, *J Chem Phys* **2013**, *139*, 084701.

[21] K. M. Neyman, S. M. Kozlov, *NPG Asia Mater* **2022**, *14*, 59.

[22] D. Gun Oh, H. A. Aleksandrov, H. Kim, I. Z. Koleva, K. Khivantsev, G. N. Vayssilov, J. Hun Kwak, *Chemistry – A European Journal* **2022**, *28*, DOI 10.1002/chem.202200684.

[23] D. G. Oh, H. A. Aleksandrov, H. Kim, I. Z. Koleva, K. Khivantsev, G. N. Vayssilov, J. H. Kwak, *Molecules* **2023**, *28*, 1957.

[24] A. Ouvrard, A. Ghalgaoui, C. Michel, C. Barth, J. Wang, S. Carrez, W. Zheng, C. R. Henry, B. Bourguignon, *The Journal of Physical Chemistry C* **2017**, *121*, 5551.

[25] M. Nolan, S. C. Parker, G. W. Watson, *Surf Sci* **2005**, *595*, 223.

[26] S. Surnev, M. Sock, M. G. Ramsey, F. P. Netzer, M. Wiklund, M. Borg, J. N. Andersen, *Surf Sci* **2000**, *470*, 171.

[27] P. Gelin, A. R. Siedle, J. T. Yates, *J Phys Chem* **1984**, *88*, 2978.

[28] A. Eichler, J. Hafner, *Phys Rev B* **1998**, *57*, 10110.

[29] K. Honkala, P. Pirilä, K. Laasonen, *Surf Sci* **2001**, *489*, 72.

[30] J. Szanyi, W. K. Kuhn, D. W. Goodman, *Journal of Vacuum Science & Technology A: Vacuum, Surfaces, and Films* **1993**, *11*, 1969.

[31] W. K. Kuhn, J. Szanyi, D. W. Goodman, *Surf Sci* **1992**, *274*, L611.

[32] P. Sautet, M. K. Rose, J. C. Dunphy, S. Behler, M. Salmeron, *Surf Sci* **2000**, *453*, 25.

[33] R. Alcala, A. DeLaRiva, E. J. Peterson, A. Benavidez, C. E. Garcia-Vargas, D. Jiang, X. I. Pereira-Hernández, H. H. Brongersma, R. ter Veen, J. Staněk, J. T. Miller, Y. Wang, A. Datye, *Appl Catal B* **2021**, *284*, 119722.

[34] F. Maurer, J. Jelic, J. Wang, A. Gänzler, P. Dolcet, C. Wöll, Y. Wang, F. Studt, M. Casapu, J.-D. Grunwaldt, *Nat Catal* **2020**, *3*, 824.

[35] G. Kresse, J. Hafner, *Phys Rev B* **1993**, *47*, 558.

[36] G. Kresse, J. Furthmüller, *Phys Rev B* **1996**, *54*, 11169.

[37] J. P. Perdew, M. Ernzerhof, K. Burke, *J Chem Phys* **1996**, *105*, 9982.

[38] S. Grimme, J. Antony, S. Ehrlich, H. Krieg, *J Chem Phys* **2010**, *132*, 154104.

[39] S. Grimme, S. Ehrlich, L. Goerigk, *J Comput Chem* **2011**, *32*, 1456.

[40] P. E. Blöchl, *Phys Rev B* **1994**, *50*, 17953.

[41] G. Kresse, D. Joubert, *Phys Rev B* **1999**, *59*, 1758.

[42] S. L. Dudarev, G. A. Botton, S. Y. Savrasov, C. J. Humphreys, A. P. Sutton, *Phys Rev B* **1998**, *57*, 1505.

[43] M. V. Ganduglia-Pirovano, A. Hofmann, J. Sauer, *Surf Sci Rep* **2007**, *62*, 219.

[44] C. Loschen, J. Carrasco, K. M. Neyman, F. Illas, *Phys Rev B Condens Matter Mater Phys* **2007**, *75*, 1.

[45] N. V Skorodumova, S. I. Simak, B. I. Lundqvist, I. A. Abrikosov, B. Johansson, *Phys Rev Lett* **2002**, *89*, 166601.

[46] M. V. Ganduglia-Pirovano, J. L. F. Da Silva, J. Sauer, *Phys Rev Lett* **2009**, *102*, 026101.

[47] S. Fabris, G. Vicario, G. Balducci, S. de Gironcoli, S. Baroni, *J Phys Chem B* **2005**, *109*, 22860.

[48] M. Cococcioni, S. de Gironcoli, *Phys Rev B* **2005**, *71*, 035105.

[49] G. Bussi, D. Donadio, M. Parrinello, *J Chem Phys* **2007**, *126*, 014101.

[50] J. Hutter, M. Iannuzzi, F. Schiffmann, J. VandeVondele, *Wiley Interdiscip Rev Comput Mol Sci* **2014**, *4*, 15.

[51] G. Lippert, M. Parrinello, J. Hutter, *Mol Phys* **1997**, *92*, 477.

ToC figure

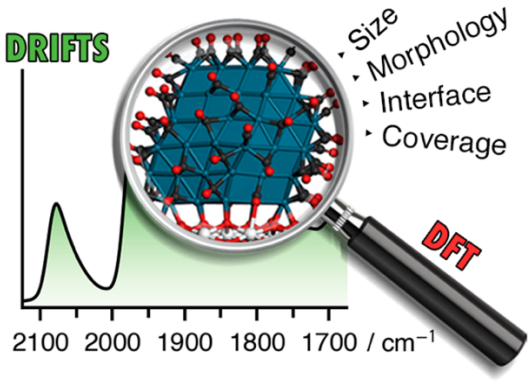
DRIFTS
Size
Morphology
Interface
Coverage
DFT
2100 2000 1900 1800 1700 / cm⁻¹